Original Article

Braze welding of cobalt with a silver–copper filler ☆

Everett M. Criss [a,*], *Marc A. Meyers* [a,b,c]

[a] *Department of Mechanical and Aerospace Engineering, University of California, San Diego, La Jolla, USA*
[b] *Materials Science and Engineering Program, University of California, San Diego, La Jolla, USA*
[c] *Department of Nanoengineering, University of California, San Diego, La Jolla, USA*

ARTICLE INFO

ABSTRACT

A new method of joining cobalt by braze-welding it with a silver–copper filler was developed in order to better understand the residual stresses in beryllium–aluminum/silicon weldments which are problematic to investigate because of the high toxicity of Be. The base and filler metals of this new welding system were selected to replicate the physical properties, crystal structures, and chemical behavior of the Be–AlSi welds. Welding parameters of this surrogate Co–AgCu system were determined by experimentation combining 4-point bending tests and microscopy. Final welds are 5 pass manual TIG (tungsten inert gas), with He top gas and Ar back gas. Control of the welding process produces welds with full penetration melting of the cobalt base. Microscopy indicates that cracking is minimal, and not through thickness, whereas 4-point bending shows failure is not by base-filler delamination. These welds improve upon the original Be–AlSi welds, which do not possess full penetration, and have considerable porosity. We propose that utilization of our welding methods will increase the strength of the Be–AlSi weldments. The specialized welding techniques developed for this study may be applicable not only for the parent Be–AlSi welds, but to braze welds and welds utilizing brittle materials in general. This concept of surrogacy may prove useful in the study of many different types of exotic welds.

1. Introduction and goals

Beryllium possesses many desirable mechanical, thermal and nuclear properties [1,2]. Chief among its superlative physical properties are high strength, high stiffness, low density, high specific heat, high melting point and hexagonal crystal structure [1–3]. Commercially it is used in beryllium–copper and beryllium oxide ceramics [4]. In pure form its use is limited to specialty applications in the defense, aerospace and energy industries due to several drawbacks, such as its low fracture strength, high cost, and toxicity [5]. In particular, the high sensitivity of Be to cracking has made welding, autogenously or otherwise, overall difficult [5]. A wide variety of

---

welding techniques have been investigated over decades, but joint quality is still highly process dependent [6]. Brazing has emerged as the most reliable and preferred process for the joining of beryllium [6]. A variation of brazing, braze-welding, is often used, in which the beryllium base partially melts [7] and is joined by silver, or aluminum based filler wire [2]. Although braze-welded beryllium structures are less susceptible to cracking, the different thermal expansion coefficients of the base and filler metals may introduce residual stresses into the part [8]. Investigation of these weldments, produced by braze-welding a Be ring with 88–12 wt.% AlSi filler, prompted the present study. Neutron beam diffraction of these welds reveals residual stress distributions inconsistent with coefficient of thermal expansion (CTE) mismatch [8], which was their expected cause. Differential heating is a possible explanation for these stress distributions, but additional study is needed to fully understand them. However, directly investigating Be–AlSi welds is limited due to the high toxicity of beryllium [9].

To circumnavigate these problems, we advance the concept of 'surrogacy', the idea that an analogous welding system can be developed and used to provide insights into the behavior of another. The purpose of our study is to develop a new welding system which will lead to a better understanding of the behavior of welds which are currently manufactured and studied at Los Alamos National Laboratory. Although this study was primarily intended to investigate the residual stresses in these Be–AlSi welds, the work done here has broader implications for other exotic weldments.

We evaluated a number of different surrogates, before selecting cobalt welded with a silver–copper filler (Co–AgCu) as our best system. Cobalt, like beryllium, has a hexagonal close packed crystal structure, a relatively high stiffness and a similar melting point [3,10,11]. Selection of this material as a base imposed a number of difficulties, mostly caused by a lack of welding information due to the infrequent use of cobalt in pure form. Worldwide, cobalt is mainly used as a constituent in batteries [12], while in the United States it is primarily used in superalloys [13]. Metallurgically it is also used in tool steels, magnets, cemented carbides, biomedical implants and wear and corrosion resistant alloys [10]. A few of these alloys utilize cobalt as their base element, and are routinely welded. Cobalt–chromium–molybdenum (Vitallium) is used in dentistry, and is generally joined via soldering or brazing [14]. However, it is also welded by torch [15] and TIG [16]. Cobalt–chromium base alloys (Stellite) are applied as hard facings using a variety of techniques such as welding, cladding and metallizing [17]. TIG may be used to apply Stellite using either helium [17] or argon shielding gas [18]. Heat resistant cobalt alloys may be welded or brazed. Welding is accomplished using a variety of techniques, including TIG, commonly with cobalt or nickel based fillers [10]. Brazing is accomplished in vacuum, or in a hydrogen atmosphere, preferably with nickel, cobalt or gold–palladium based filler metals [10].

The behavior of these alloys differs substantially from that of pure cobalt, such that the welding parameters for our system had to be independently determined. Welding was investigated in an extensive, multi-parameter study where weld quality was evaluated by four-point bending, SEM and optical microscopy. In order to satisfactorily join our materials, we developed novel methods of welding by hand, including alternating welding direction, adopting unusual weld bead placements, and welding on top of a refractory material. Finally, our failures in 4-point bending were investigated by finite element analysis (FEA). Although our welding parameters differ substantially from the original Beryllium welds, we believe the techniques developed here are applicable to Be–AlSi welds and braze welds in general, due to the careful selection of our surrogate materials.

2. Surrogacy

2.1. Surrogacy criteria

As detailed below, we selected cobalt, braze welded with 72–28 wt.% AgCu as an optimal surrogate for beryllium weldments. To mimic the residual stresses, failure mechanisms and overall weld behavior, the entire weld system must be surrogated. Selection of a reasonable surrogate insures that the techniques used to join our welds will be applicable to the original system. The quality of our surrogate is not entirely dependent on the material properties of either the base or the filler, but also upon their interactions. Our Co–AgCu combination was selected to mimic the key traits of the Be–AlSi system, including base and filler properties, as well as their chemical interactions. This approach allowed the determination of a list of core requirements for our surrogate welding system (Table 1) [3,19–21]. In order to form the core criteria for our filler, approximating the filler properties was necessary. This was done using the Voigt–Reuss–Hill average of the filler's constituent polycrystalline elastic modulus (E) [e.g. 22]:

$$E \approx \frac{1}{2} \left(\frac{1}{\sum f_i/E_i} + \sum E_i f_i \right) \qquad (1)$$

where E_i is the elastic modulus of an individual component and f_i is the volume fraction of that component. This equation was modified *mutatis mutandis* for the coefficient of thermal expansion (α), resulting in:

$$\alpha \approx \frac{1}{2} \left(\frac{\sum f_i E_i \alpha_i}{\sum f_i E_i} + \sum f_i \alpha_i \right) \qquad (2)$$

where the symbols are as above and α_i is the thermal expansion coefficient of the component materials.

Although better approximations are possible, the allowable ranges of our core criteria are sufficiently large that the errors in these calculations are not significant. We then utilized these criteria to select possible surrogate base metals, and to select compatible fillers.

2.2. Base surrogacy

The behavior and material properties of beryllium are highly influenced by its hexagonal close packed (HCP) structure and anisotropic lattice, which provides it with the lowest *c/a* ratio of any *hcp* element [5]. The requirement for our surrogate system to have an HCP base imposes strong limitations on

Table 1 – Core criteria for the surrogate welding system.

	Priority	Be–AlSi	Co–AgCu
Core criteria (base)			
Safe to weld	1	No	Yes
Hexagonal base	2	Yes (P6$_3$/*mmc*)	Yes (P6$_3$/*mmc*)
Obtainable, less than $500/kg	3	No ($235.89/kg)	Yes ($45.97/kg)
895 °C < base MP < 1680 °C (within 25%)	4	Yes (1287 °C)	Yes (1495 °C)
Core criteria (system)			
Safe to weld	1	No	Yes
Immiscible base/filler	2	Yes	Yes
1.25 < filler CTE/base CTE < 2.75	3	Yes (1.95)	Yes (1.38)
2 < base E/filler E	4	Yes (4.24)	Yes (2.22)
30% < filler M.p./base M.p. < 80%	5	Yes (54%)	Yes (60%)

potential surrogates, as very few room temperature HCP elements are both obtainable and safe to weld. Of these materials, zinc was excluded due to its low melting point, and zirconium due to its excessive melting point.

Our criteria (Table 1) suggest that only two options, cobalt and titanium, are viable. We also include magnesium for reference due to its chemical similarity to beryllium in spite of its comparatively low melting point (650 °C) and combustible nature.

Table 2 [3,23] compares the properties of Be, Co, Ti and Mg that are most likely to influence residual stresses inside a weld. This comparison shows that cobalt has the mechanical properties most similar to beryllium, although magnesium is the best thermal match. However, no viable fillers were found for Mg (see below) and magnesium's high ductility and low stiffness make it a difficult beryllium surrogate, whereas the mismatched thermal properties of cobalt can be mitigated by varying welding techniques. Based on material properties alone, cobalt appears the most reasonable beryllium surrogate.

2.3. Filler surrogacy

The Be–AlSi system is characterized by the immiscibility of its primary constituents (Table 3) [24–35]. In order to replicate the behavior of the Be–AlSi system, it is necessary that our system also be characterized by base-filler immiscibility. No suitable filler metals were found for either Ti or Mg. The melting point of magnesium is too low for any feasible filler, while no potential titanium fillers conform to all of our criteria.

Cobalt is immiscible with a handful of elements, among them copper, silver, gold and lead. Gold must be discounted due to cost, and lead lacks a melting point high enough to function effectively as a filler metal. However, silver and copper are relatively inexpensive and easily obtainable as filler wire, due to the prevalence of silver soldering. This availability prompted our choice of cobalt as an ideal material for beryllium surrogacy

Silver was selected as a filler over copper, because it has a CTE ratio further from cobalt, potentially producing higher stresses [3]. However, preliminary welding studies indicated that pure silver is not capable of forming strong welds with cobalt. To correct this deficiency, Ag was alloyed with 28 wt.% copper [21]. Material properties of this Co–AgCu surrogate alongside the original Be–AlSi system are provided (Table 4)

[3,20,21]. This surrogate system exceeds all of our original requirements (Table 1). Furthermore, the chemistry of our surrogate system resembles the phase stability of the original Be–AlSi system (Table 3).

However, the chemistries of the base and surrogate systems differ in one important regard: the limited miscibility between liquid cobalt and liquid silver (monotectic response) leads to Co-Ag phase separation. This difference is unavoidable, and results in microstructural differences near the filler–base interface, due to the lack of a eutectic point between silver and cobalt.

3. Experimental techniques

3.1. Materials

The base material was 99.95% pure cobalt (Sophisticated Alloys). Prior to welding, Co was hot rolled to 7.6 mm and heat treated at either 325 °C or 350 °C for 100 h to homogenize the grain structure of our metal. However, some studies [36] have reported the persistence of the FCC phase after refining the grain structure by rolling. In order to ensure that no FCC material was present, the cobalt was again heat treated at either 350 ± 10 °C or 325 ± 10 °C at 100 h, and then allowed to slowly cool. For the second heat treatment, the temperature was measured at various locations to ensure consistency.

The filler selected was 72–28% AgCu wire (Lucas Milhaupt), which is at the eutectic point.

3.2. XRD characterization

One of the heat treated blocks and an unheated blank were sectioned to expose three orthogonal faces. X-ray diffraction was performed with a Rigaku Geigerflex D-MAX/A Diffractometer at Washington University in St. Louis using Cu Kα radiation. We used 35 kV and 35 mA. No noticeable FCC peaks were found on any of these 6 faces, allowing the conclusion that neither treatment nor hot rolling had induced any persistent FCC structures significant to these experiments.

3.3. Fracture in 4-point bending

Quality of these welds was determined by fracture in a 4-point bending apparatus, connected to an Instron 3307 tensile tester. To perform these tests, the welds are cut into 8 parts; 2 end

Table 2 – Relevant properties of potential base elements.

Relevant material properties	Beryllium	Cobalt	Magnesium	Titanium
Young's modulus, GPa	318	**211**	44.7	120.2
Poisson's ratio	0.02	0.32	**0.291**	0.361
CTE, 25 °C, μm/m °C	11.3	**13.0**	24.8	8.6
Melting Pt., °C	1287	**1495**	650	1668
HCP-FCC transition	1270	422	N/A	**882**
Conductivity, W/m K, 25 °C	210	69.04	**155**	11.4
Specific heat, J/g °K, 0–100 °C	1825	421	**1023**	523
Lattice c/a ratio	1.5681	1.6228	1.6236	**1.5873**
Density, g/cm^3 20 °C	1.85	8.86	**1.74**	4.51
Immiscible fillers[a]	Al, Ag, Si	Ag, Au, Cu		Si, V

Bold values are most similar to beryllium.

[a] Fillers shown are immiscible, commercially obtainable as a primary or secondary constituent in filler wire, and between 50% and 125% the base material's melting point.

Table 3 – Characteristics of Be–AlSi and Co–AgCu alloy systems.

	Al–Si	Al–Be	Be–Si	Ag–Cu	Ag–Co	Co–Cu
Type	Filler	Base-filler 1	Base-filler 2	Filler	Base-filler 1	Base-filler 2
System	Eutectic	Eutectic	Eutectic	Eutectic	Immiscible	Peritectic
Eutectic point	12.2 at.%. Si	2.4 at.% Be	36 at.% Si	39.9 at.% Cu	N/A	N/A
Eutectic temp[a]	577　575	644	1085　1090	780　782	N/A	N/A

[a] Left value is experimental, right is a calculated equilibrium value. Both sources are in agreement for Al–Be.

Table 4 – Relevant properties of fillers, and their constitutive elements.

	Al	Si	Al–12Si	Ag	Cu	Ag–28Cu
Young's modulus, GPa	70.6	113		82.7	129.8	
E, Voigt–Reuss–Hill avg			75			95
Poisson's ratio	.345	.42		.367	.343	
CTE, 25 °C	23.1	7.6		18.9	16.5	
CTE, Voigt–Reuss–Hill avg.			22			18
Melting Pt.	660.323	1412	577–582[a]	961.78	1084.62	780
Conductivity, W/m K, 25 °C	247	156		428	398	
Specific Heat J/kg K, 25 °C	897	705		235	385	
Specific heat, average			874			277
Density, g/cm^3	2.7	2.34		10.5	8.96	

[a] Solidus and liquidus temperatures.

pieces and 6 samples (Figs. 1 and 2). The end pieces were not used due to the unstable nature of the transient region. The asymmetrical sectioning (Fig. 1) reflects our estimation of the location of the quasi-steady zone. Sample 3 was not usually fractured, but was instead preserved for microscopy.

We also performed 4-point bending tests on four samples, made from our pre-welded, heat treated cobalt block, to compare the quality of our welds to the parent material. These samples have the same single-U geometry as our welds, but are cut out of a single piece of cobalt (Fig. 3).

The orientation of the welds during fracture (Fig. 3) was selected such that fracture would occur at the base of the weld. This orientation corresponds to the expected failure direction due to the residual stresses induced by CTE.

The bending apparatus was set to have a 48 mm support span, and a 12 mm load span. The load span was chosen to be slightly larger than the expected width of the weld pool, while the support span was as wide as our weld geometry would allow (Fig. 3). No extensometer was employed during

the tests, resulting in data that are accurate for loads, but provide displacements that are generally overestimated.

3.4. Optical microscopy

Optical microscopy was performed on chemically etched samples in order to reveal both the microstructure and macrostructure of the welds. Two etchants were sequentially used. The first etch was composed of a solution of 60 ml hydrochloric acid, 15 ml nitric acid, 10 ml water, and 15 ml acetic acid The sample was then placed in a secondary solution of 60 ml nitric acid and 40 ml methanol which was slowly diluted by a 1–1 water–methanol mixture before being quenched by water (modified from Ref. [37]). All images were produced on faces located exactly 40.6 mm from the weld start (Fig. 4).

Etching using this procedure was performed on all of the intermediate stages of the weld. These images were taken
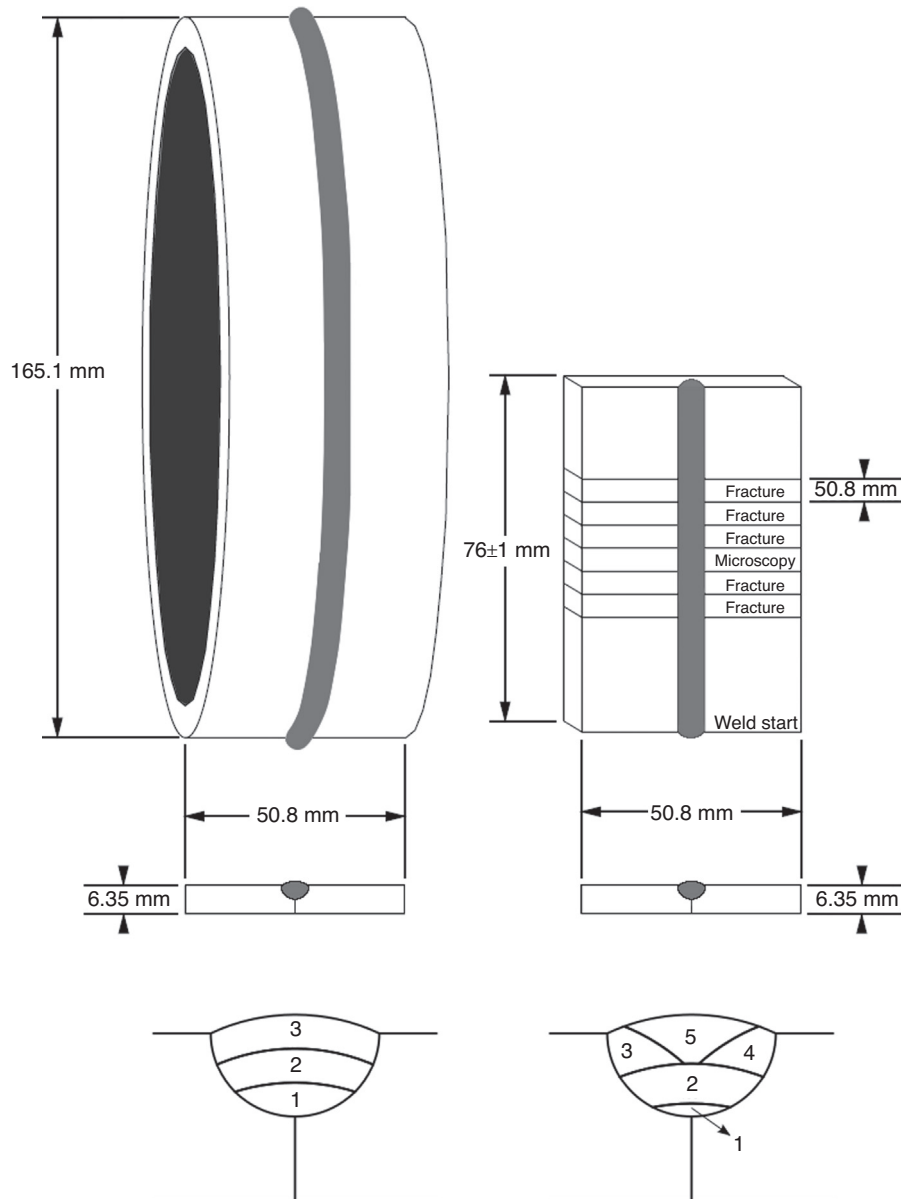
Fig. 1 – Weld schematics. (Left) PIGMA welded Be–AlSi weldment. (Right) TIG welded Co–AgCu weldment. Schematic shows weldment geometry and approximate pass locations for both the Be–AlSi and the Co–AgCu weldments, as well as the locations for our fracture and microscopy samples. The samples (right) are all undersized by approximately .35 mm due to the width of the wire in our EDM. Dimensions are all ±08 mm unless noted otherwise. Image of Be ring modified from [8].

with indirect light using digital color inversion (Fig. 4, left column), and direct light (Fig. 4, middle column).

3.5. Scanning electron microscopy (SEM)

SEM was performed on a Phillips XL30 ESEM with an Oxford EDS attachment. Images were taken after etching as described above. No coating was used.

3.6. Welding equipment and materials

Optimization of weld parameters requires consistency. In order to reduce uncertainty, all welds were produced by the same ASME aerospace certified welder on a TIG Welder with high frequency stabilization (Miller Aerowave) set to direct current electron negative (DCEN).

The standardized weld part used in this study was a 76 mm long, 25.4 mm wide, 6.25 mm thick block of 99.95% cobalt with a 3.2 mm radius J-groove (Fig. 1). These parts were precision machined, so that the thicknesses of the J-groove and part were accurate to 0.08 mm.

Our parts were held with a specially built clamp during welding, which rigidly positioned the cobalt plates above a crushed refractory substrate. This permitted argon back-gas to shield the weld, while still reflecting heat back onto the weld base.
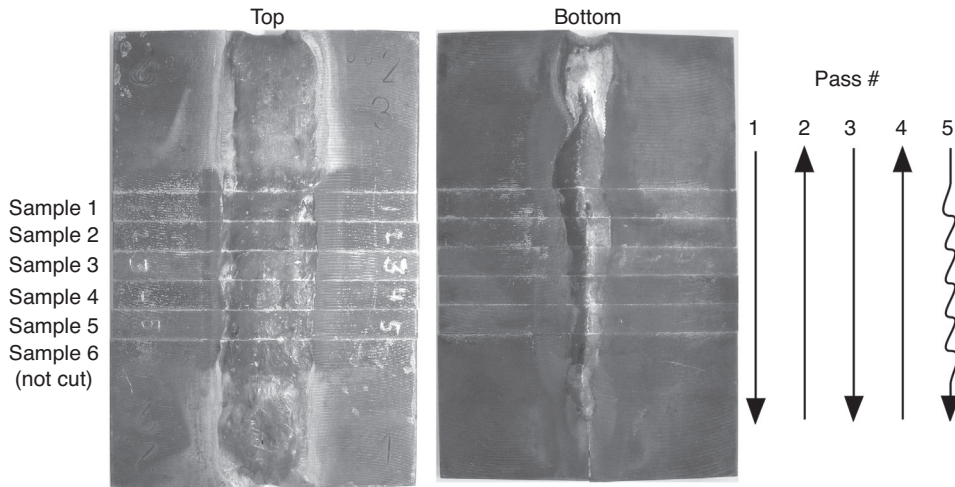
Fig. 2 – 5 pass weld showing sample locations and welding direction. Top and bottom images of a 5 pass weld. Sample 6 has not yet been cut. Notice the large weld pool at the start of the weld, tapering away toward the base. This shape has been observed in a large percentage of our welds, and indicates the welding power was too low. The alternating welding direction was selected in order to minimize thermal gradients due to our small weld length. The final oscillating 'filler' pass was designated by a wavy line.

3.7. Finite element analysis

Models of the fracture tests were created in Abaqus from microscopic images (Fig. 3, bottom, Fig. 4, right column). These finite element analysis (FEA) models are two-dimensional, assume plane stress, and apply loads via frictionless contact with 4 rollers (Fig. 3). The model is displacement controlled in order to reduce instabilities. The four rollers are assumed elastic, whereas the sample and filler are assumed to follow metal plasticity, as defined by Abaqus using the von Mises yield surface. The standard, implicit problem solver was used,

with a maximum time step corresponding approximately to a deflection of 5×10^{-4} mm.

Geometry was extrapolated by manually outlining the images, and converting this outline to a DXF file. This outline was then uploaded into Abaqus, where it was scaled and rotated into position. Mesh sizes in the sample varied slightly, but corresponded to a seed length of 0.1 mm (Fig. 3, bottom, Fig. 4, right column). Mesh sizes in the rollers were coarser, which is of little consequence because the material is assumed to be elastic.

To replicate 4-point bending, the model assumes that the bottom rollers are stationary, and the top rollers are capable of motion only along the Y (vertical) axis. The 4-point bending is modeled as contact between the plastic ('slave') sample surface, and the elastic ('master') roller surface, and assumes a frictionless interface. The sample is locked in place by assuming that the node at the base of the weld pool is stationary. The simulation was displacement controlled, and was ended when the maximum nodal stress exceeded the von Mises failure stress of cobalt.

Material data for AISI 304 steel rollers was provided by Smithells [3], while plasticity data for the other materials was extrapolated from published experimental results [38,39]. This extrapolation was done by assuming that the true stress (σ_t) and true strain (ε_t) are related to engineering stress (σ_E) and measured strain (ε_m) by
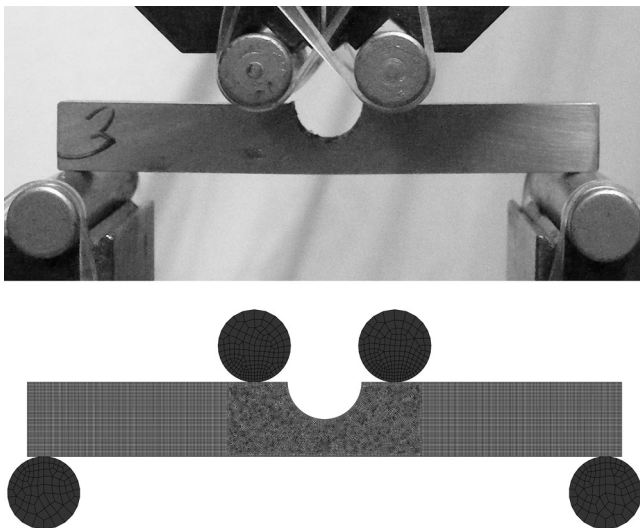

Fig. 3 – Fracture setup, and its corresponding FEA. Photograph captures our 4pt bending apparatus fracturing a blank specimen, while the computer image shows element size and orientation in our FEA. Fracture Setup is intended to mimic "natural" failure of the welds, due to CTE mismatch and expected grain orientation.

$$\sigma_t \cong \sigma_E(1 + \varepsilon_E) = \sigma_E \left(1 + \varepsilon_m - \frac{\sigma_E}{b}\right) \tag{3a}$$

$$\varepsilon_t \cong \ln(1 + \varepsilon_E) = \ln\left(1 + \varepsilon_m - \frac{\sigma_E}{b}\right) \tag{3b}$$

where b is the spring constant of the testing machine. These equations assume incompressible materials, and a linear deflection of the testing machine with load. In order to calculate these results, the Young's modulus of cobalt was assumed
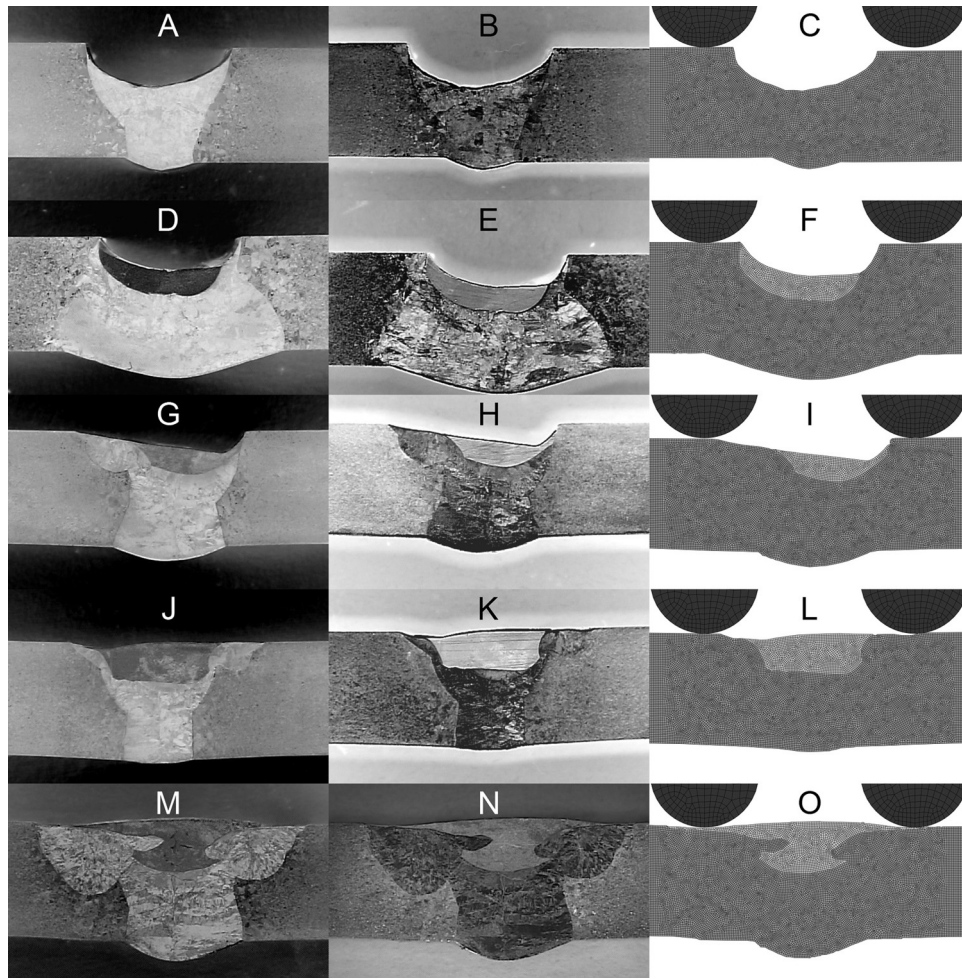
Fig. 4 – Welds sectioned at increasing number of passes. Microscopic images using diffused light and color inversion are shown to the left; direct light is in the middle, and the corresponding FEA model is to the right. The FEA models contain the base, as well as two of the rollers used in four point bending. In all images, the silver filler is located up. The different colored area surrounding the filler in the microscopic images is the cobalt, which has been melted. The areas on either side of the melted region is the HAZ, which exhibits grain growth. All welds contain backfilled cracks, but they are most obvious in welds 2 (DE) and 5 (MN). All welds show grain growth originating at the center. Close inspection of the images shows an area immediately under the filler pool, which forms an arc. This area is most visible in G and H; it is suspected the different grain structure is due to the formation of a Cu–Co alloy.

to be 211 GPa [3] while silver–copper was assumed to have a Young's modulus of 95 GPa (Table 4), calculated as an approximate midpoint between the Reuss and Voigt averages for these materials. These assumed values for the moduli allowed calculation of the true stresses and strains from reported data by solving for the spring constant using only data from the elastic region and the equation

$$b \cong \frac{\sigma_E^2}{\sigma_E \varepsilon_m + EW(-\sigma_E/b) + \sigma_E} \tag{4}$$

where W is the Lambert function:

$$W(z)e^{W(z)} = z \tag{5}$$

Using these equations, tensile results for AgCu and annealed cobalt were transferred into true stress and strain (Fig. 5), and input into Abaqus.

4. Welding methodology

4.1. Welding parameter determination

The techniques used in welding beryllium provided the basis for initial attempts at joining our surrogate. However, differences in the systems described in Section 2 required development of an entirely new welding system with specialized techniques. However, these techniques should be applicable to the original Beryllium welds, due to the physical similarities between these systems.
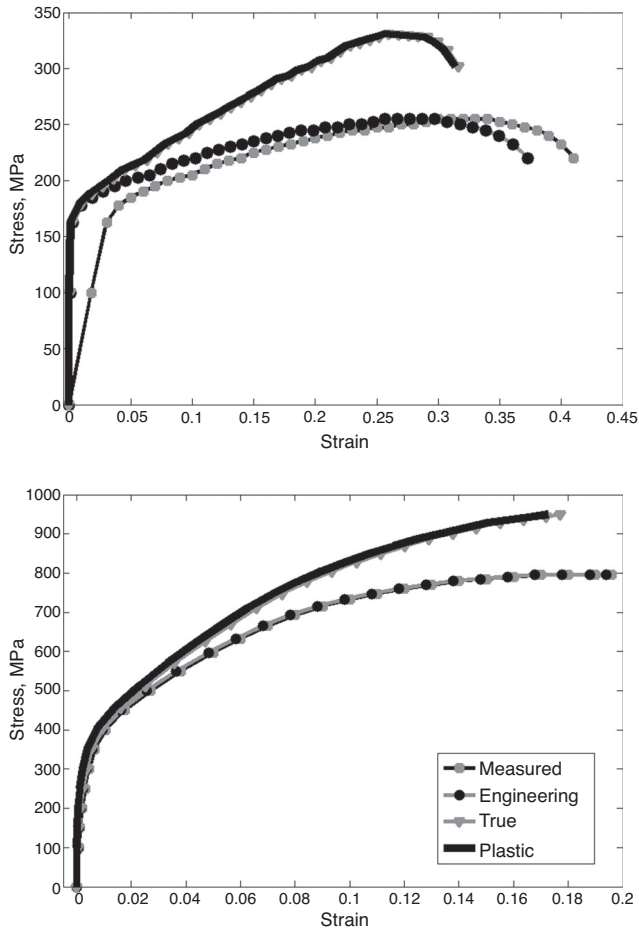
Fig. 5 – Calculated stress vs. strain curves. Raw data taken from literature and subjected to Eqs. (4) and (5). Deviations between engineering and measured stress–strain curves due to machine flexure; deviations between engineering and true stresses due to 'necking'. Plastic stress, used in our FEA models, is true stress minus elastic strain.

Determination of weld parameters involved an extended multi-parameter study. Effects of top gas, back gas, amperage, pass number and position, and various clamping techniques were investigated. A majority of these welds were discarded after visual inspection, due to incomplete melting. Weld quality of the remaining samples was evaluated with a combination of optical microscopy and 4-point bending. Since one of the goals of this study is residual stress analysis, our welds were evaluated based not only on their strength in 4-point bending, but also on the consistency of the individual samples. Thus, welding techniques that ensure full thickness melting, and crack mitigation were preferentially selected. This was not a straightforward procedure, as techniques that increase weld penetration generally also result in more cracking.

Final welding parameters were evaluated through fracture, optical microscopy and SEM. Furthermore, FEA was performed in order to supplement our fracture results. These tests were performed on a complete weld, and on a series of incomplete welds after every pass.

Table 5 – Welding parameter comparison.		
Welding parameters	Be–AlSi	Co–AgCu
Base metal crystal structure	HCP	HCP
Filler metal crystal structure	FCC-diamond	FCC
Immiscible constituents	Yes	Yes
Welding method	3 pass MIG	5 pass TIG
Geometry	Cylindrical Double J groove	0.25″X1″X3″ plate Double J groove
Shielding gas	0.39 helium–.07 argon	0.43 helium topgas, 0.25 argon backgas
Maximum amperage (A)	150	225[a]
Voltage (V)	21.8	60 (90)[b]

[a] Foot pedal controlled.
[b] Maximum voltage (maximum start voltage).

4.2. Final welding parameters

Our final manual tungsten inert gas (TIG) welding parameters used 5 passes with alternating directions. This unorthodox approach was adopted after we observed that welding in alternating directions resulted in a more consistent weld pool, smaller transient areas at the beginning and end of the weld, and a larger quasi-steady zone. The first four passes were done at 225 A, with 0.43 l/s He top-gas and 0.25 l/s Ar back-gas, while the final pass was done at 150 A with 0.25 l/s Ar top-gas and back-gas. The weldments were allowed to cool to room temperature between passes for all but the first two.

The clamp (Section 3.5) was heated prior to welding inside a muffle furnace to above 300 °C. The clamp was then air-cooled to 250 °C before the part was loaded. Welding occurred at a substrate temperature of approximately 230 °C, which was monitored by a thermocouple. Furnace heating the clamp significantly improved the consistency of latter welds; however only pass 5 was produced this way. Passes 1–4 were instead produced on a clamp preheated by previous welds.

These parameters are significantly different from those used to produce Be–AlSi welds at Los Alamos National Laboratory (LANL). Those welds are 3 pass metal inert gas (MIG), robotically welded in an Ar–He environment. The base is S200D grade beryllium, formed into two 165.1 mm diameter rings, 6.35 mm thick, 25.4 mm high with a 3.18 mm J groove (Fig. 1) [8]. Our welding parameters are compared with the LANL Be parameters in Table 5 [8,40]. More significant than our geometrical differences was our substitution of TIG for the MIG welding used on beryllium (Table 5). By replacing TIG with MIG we were able to form coherent welds, due to the greater amount of energy TIG imparts to the weld base.

Producing these welds by hand implies that the currents used in these experiments do not provide an accurate measure of the energy imparted to the weld. Since the welder controls the power of the torch, the values given here correspond to the maximum current available. This is only achieved when the foot-pedal is fully depressed. Generally, full power is only used for the first pass. Repeated trials resulted in our selection of a 225 A limit. However, recording and analysis of power data, done after this study, suggest that 225 A may be below the optimum amperage.

Hand welding introduces additional uncertainties as well, since the torch position, feed rate, and traverse speed are not precisely controlled. This is beneficial in the prototyping phase, allowing a human welder much greater flexibility than a machine. Unfortunately, this complicates analysis since the welds are less consistent. Further study has concentrated on thermal profiles and power usage; information necessary for automation. Our techniques have proven consistent enough for us to generate 13 additional 5-pass welds for further study.

5. Results and discussion

Weld quality was evaluated using a combination of 4-point bending, microscopy, and FEA. These evaluations were performed on a complete 5 pass weld, and a series of incomplete welds, halted after passes 1–4. This allows investigation into the quality of the individual passes. A 4-point bending apparatus was used to evaluate weld quality, since it produces failure which would be most augmented by CTE mismatch. Optical microscopy allows analysis of grain structure, cracking and overall quality, while SEM shows the fine structure and material composition. Finite element analysis allows interpretation of fracture results.

5.1. Microscopy

The optical images were taken with direct (Fig. 4, middle column), and indirect light (Fig. 4, left column), the latter using digital color inversion. These images show a high variability in the size of the melted cobalt regions, as well as a sizable reduction in the size of the filler pool, when compared to the machined shape (Figs. 3 and 4). This change is due to melted cobalt flowing toward the weld base, and to AgCu going into solution with the cobalt. The variability in shape of the melted zone illustrates the inherent uncertainty of hand-made welds. Furthermore, this uncertainty is such that the effect of the 2nd pass on weld geometry is not possible to determine; although its impact must be slight (Fig. 4d–f). The 3rd and 4th passes melt only a semicircular area on the side of the weld (Fig. 4g, h, j and k). Of note are the elongated (columnar) grains with the long axis pointing toward the center, which is most clear in the image of pass 1 (Fig. 4b) and pass 5 (Fig. 4m), although it is present in all passes. This is significant, as the center line into which grains converge facilitates cracking in the weld center (Fig. 6f), since impurities segregate in the molten pool. The 5th pass, is produced with a lower temperature arc, with the intention of filling any low areas left after the 4th pass. The markedly different shape of the 5th pass is thought due to the

weld experiencing very hot 3rd and 4th passes as evidenced by the large melted regions.

The micrographs show that the completed weldments contain 5 distinct regions. The unaffected cobalt is characterized by the small grain size ($\approx$20 μm) produced by rolling (Fig. 6a) and is located away from the weld. The heat-affected zone (HAZ) is visible in all images on both sides of the weld (Fig. 4), although its extent can only be determined by comparing both the images produced with direct (Fig. 4, middle column) and indirect light (Fig. 4, left). This region exhibits grain growth. The weld pool is characterized by larger grained cobalt ($\approx$500 μm), coupled with backfilled silver–copper cracks (Fig. 6f). At the top is the AgCu eutectic, which is occasionally invaded by cobalt nodules (Figs. 6b and 7a). The eutectic is composed of large dendrites, surrounded by a much finer region (Figs. 6b and 7a). The complete lack of solubility between cobalt and silver results in a sharp base-filler boundary (Fig. 7a–c). Occasional cobalt and silver particles migrate, appearing as small silver 'drops' in the cobalt (Fig 7a and b), or as cobalt nodules in the filler (Fig. 7a, b and d). Copper, however, enters the cobalt base in quantity (Fig. 7c). This miscibility is thought to cause the final weld region; a small, arcuate area most visible in pass 3 (Fig. 4g and h), although it is thought present in all images. Magnification of this region (Fig. 6c–e) seems to show a fine, reticulated structure, presumably from Co–Cu phase separation.

5.2. Fracture testing and FEA

Finite Element Analysis was used to evaluate our fracture results. The experimentally obtained (after stiffness correction) von Mises stress at failure of cobalt was approximately 950 MPa. Finite element modeling shows the influence of stress concentrations (Fig. 8) on fracture location. Higher numbers of passes resulted in predicted fractures on either side of the weld base, whereas fewer passes produced failure at the top of the weld pool. The failure initiation regions are marked by arrows (Fig. 8). However, experiments show that failure is generally observed in the center of the weld, due to local cracks produced by the convergence of grain boundaries.

Four-point bending, as described in Section 3, was performed on the outside 5 pieces for the intermediate and final stages of the weld (Fig. 3). These moment vs. displacement plots are normalized to the width of the samples, and compared to crosshead displacement of the tensile tester. This was done to eliminate any effects caused by inexact sectioning. The most important trends in these plots are the general increase in strength with the number of passes. The increased strength is expected and is caused by the addition of material to the welds.

All specimens fail at a higher displacement than predicted by FEA (Fig. 9) and all welds (Fig. 9, passes 1–5) exhibit lower than predicted force vs. displacement curves. These effects may have a number of physical causes, such as presence of Ag cracks in the cobalt base, large grain sizes, or slip and deflection of the tensile tester itself. The simulation, which truncates due to predicted local failure, may also contribute to this effect by ending prematurely. The higher than predicted force vs. displacement curves of the cobalt blanks are probably due to their finer grain size.
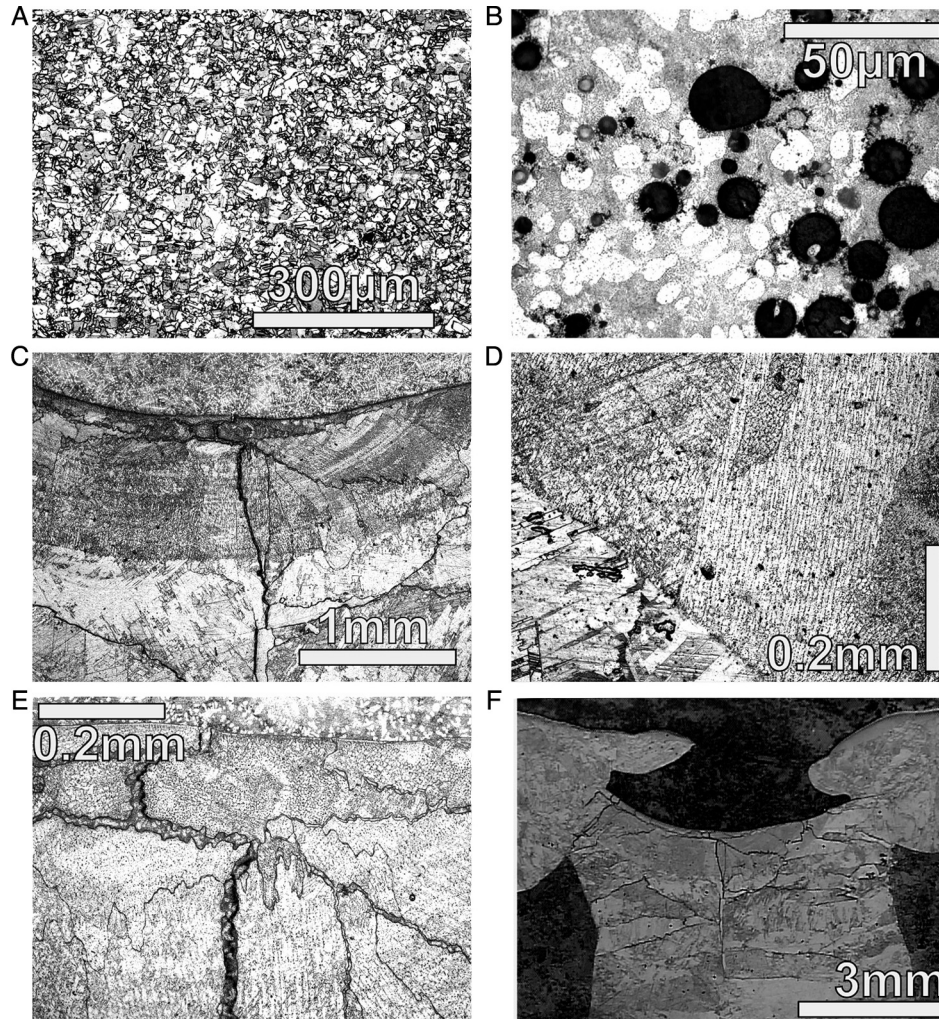
Fig. 6 – Optical Micrographs. Taken from pass 5, unless noted otherwise. (A) Base grain structure of pure cobalt, far from the weld. Note the small, consistent grain size, produced by the rolling of our base. (B) Image inside the filler showing the AgCu eutectic (white and tan). The dark areas are cobalt grains, which has been verified by SEM (Fig. 7). From a prior 5 pass weld. (C) The AgCu filler (top) is bounded by an arcuate region below it, also visible in Fig. 3, rows 3–5. This region is thought to contain significant amounts of copper. Below this region is the cobalt base consisting of hcp grains meeting at a central crack. (D) A magnified image showing the probable intersection of the Co base, and a CoCu mixture. Filler is up, and off-screen. The cellular structure is thought to be produced by Cu exsolving from the Cobalt base. From pass 4. (E) A magnified image showing the intersection of the AgCu filler, and the CoCu mixture. The AgCu dendrites are located at the top. Below this is another, finer, dendritic structure, thought to be caused by copper exsolution. Several backfilled cracks are present in the middle of the image. Some of the small dots in this image seem to be silver, isolated inside the cobalt base. (F) Cracks enhanced optically. The network of backfilled cracks originates at the filler, and grows outward from a predominant, central crack. This behavior has been observed in all welds, and is one of the primary factors affecting weld strength. Also, note the small crack, running directly under the filler. This crack is due to CTE mismatch, and has also been repeatedly observed.

Further analysis of these welds involved determination of the quasi-steady region of the samples. This was done by comparing the initial stiffness and maximum applied loads and deflections. Determination of the stiffness involved finding highest slope in the load vs. deflection graph. This was done in order to avoid the "ramping up" often seen in tensile testers. The stiffness is seen to increase with the number of passes, and is roughly constant inside all weld stages (Fig. 10).

Sample stiffness is useful for determining the quasi-steady state region of these welds, as it is heavily dependent on macro geometry. Although effects such as residual stresses or cracking may play a prominent role in weld failure, the purely elastic response will largely ignore them. Thus, these stiffness plots indicate whether the geometry is fairly consistent inside the welds; one of the features of the quasi-steady state region.

Interestingly, the weld with 5 passes has a less consistent, and often lower stiffness then the weld with 4 passes. This may be due to the presence of backfilled cracks, or geometric differences due to the tapering weld pool (Fig. 2). In either case,
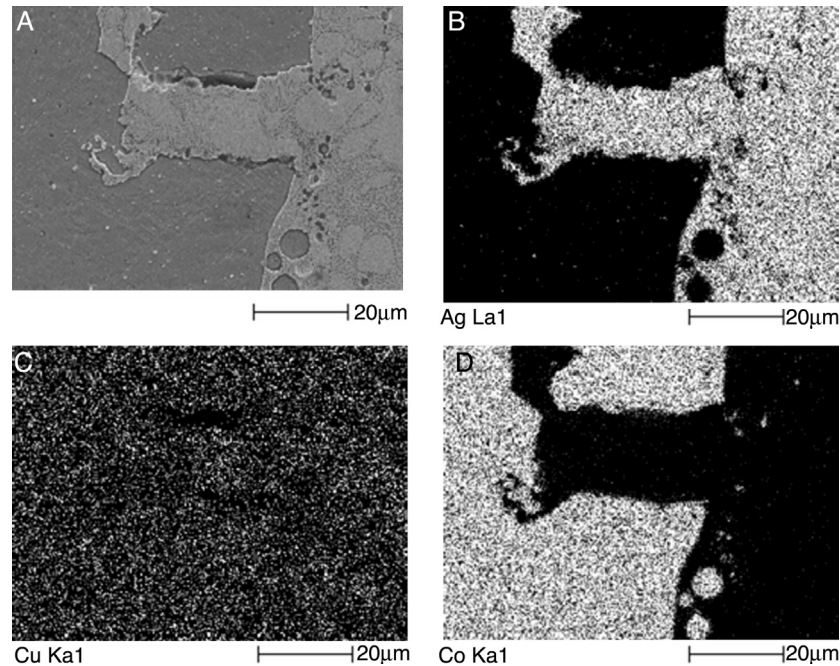
Fig. 7 – SEM backscatter and EDX images of the weld-filler interface. Images taken on the 5 pass weld after chemical etching. (A) SEM backscatter shows the intersection between the cobalt (dark gray) and the silver copper (light gray and dendritic). Note the presence of cobalt inside the filler (dark, circular grains), and small concentrations of silver inside the cobalt base (white spots). The extremely dark areas along the interface are voids. These voids were probably caused by hot shortness, and may have been augmented by the chemical etch. (B) Silver (Ag) EDX scan shows the lack of mixing between the silver in the filler (right) and the cobalt base (left). (C) EDX scan for copper shows a nearly universal distribution of copper, indicating that cobalt and copper went into solution with the cobalt during welding. There appears to be a slightly higher concentration of copper inside the globular grains in the filler, indicating that the fine, dendritic area is the eutectic, and that the filler in this image is copper rich. (D) Cobalt EDX scan shows the lack of mixing between the cobalt and silver constituents. Confirms that the inclusions in the filler are cobalt.
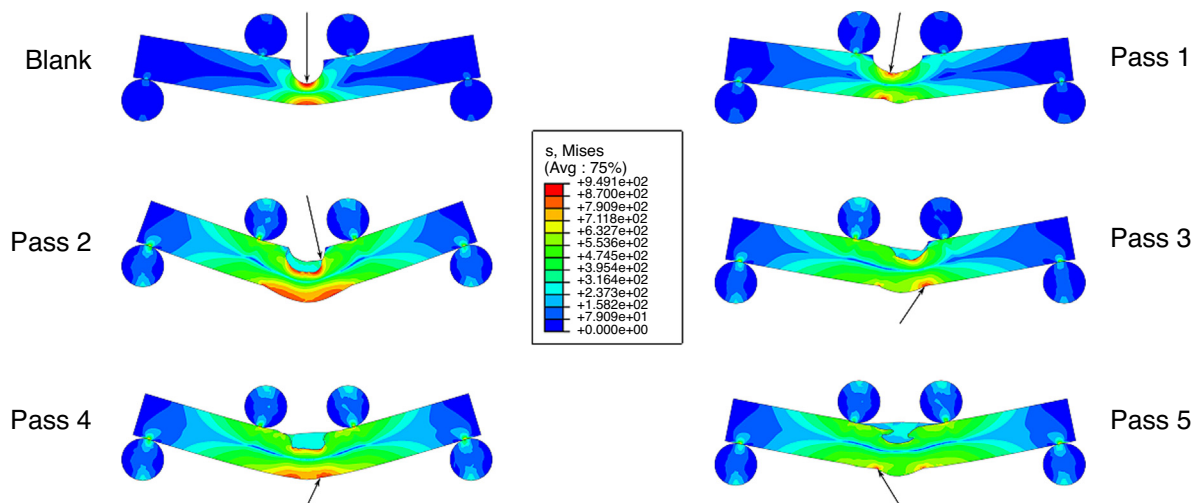

Fig. 8 – von Mises stresses at failure. Images show predicted stress field at minimum displacement sufficient to cause material failure according to the von Mises yield criterion. (von Mises failure stress is assumed 949.08 MPa.) The location of the peak stress is designated by the arrow. Note how the location at failure changes from the top of the sample, for low numbers of passes, to the bottom of the sample, on one side of the weld pool. This observation is crucial, as weld failures have been observed both here, and at the center of the weld. This indicates that these welds have been weakened by cracking, but that this is highly mitigated since the cracks are not in the regions of highest stress. Also note the large stressed areas in pass 1 and pass 3, indicating that the stress concentrations for these samples is lower.
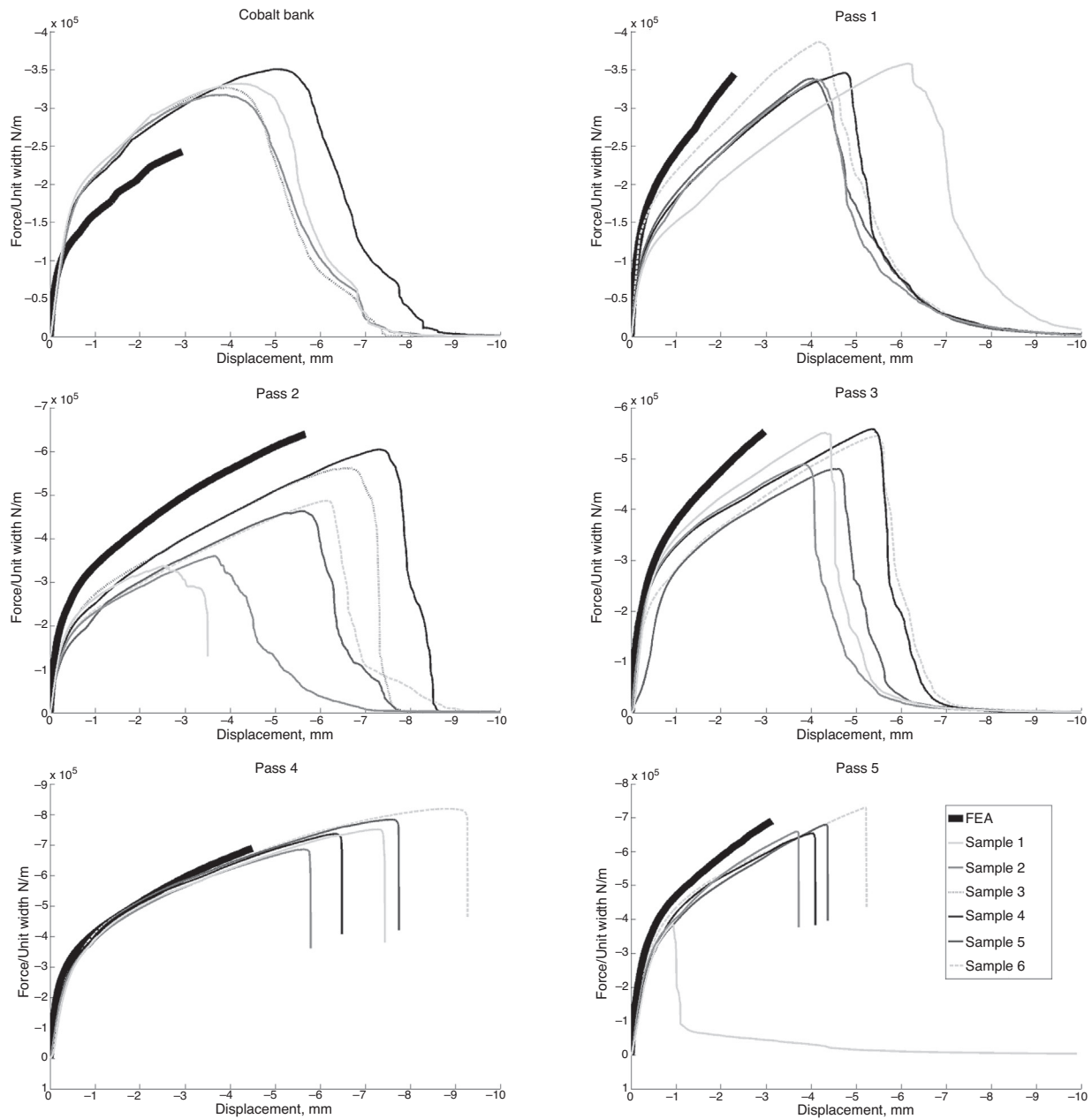
Fig. 9 – Applied load vs. displacement curves for fracture specimens and FEA models. The load is normalized by the sample width, or for the FEA curves, the section width. The displacement is measured at the tensile tester's screw, and modeled as the displacement of the top rollers. Note the average increase in failure moment at the number of passes increases. Also, note the increased severity of failure as the number of passes increases. This is most noticeable in pass 4 and pass 5, where the machine truncated the test due to the abrupt change in load. The overestimation of load by FEA is thought to be mostly caused by dissimilarities between the theoretical and actual materials, although slip and flex of the tensile tester could contribute. The opposite behavior of the cobalt blank is due to the material composing the blanks not being softened by the welding process. The underestimation of displacement at failure may be caused by the truncation of the simulation before total failure and by the slip of the tester.

the AgCu overfill (Fig. 4m, n and o) seems to not significantly stiffen the weldment.

Sample 1 often has a higher stiffness than the other samples. This is probably due to the first sample being on the edge of the initial weld pool. What follows is a 20 mm long area of fairly consistent geometry, for all but the 3-pass weld. It is likely the variations seen in the 3-pass weld are augmented by

its asymmetric section (Fig. 4g, h and i). The final sample position indicates an increase in stiffness for three of our welds, which may be an effect of the weld pool at the back of the weld.

The conclusion that samples 1 and 6 are outside the quasi-steady state region is supported by both the load vs. sample position and displacement vs. sample position plots (Fig. 11).
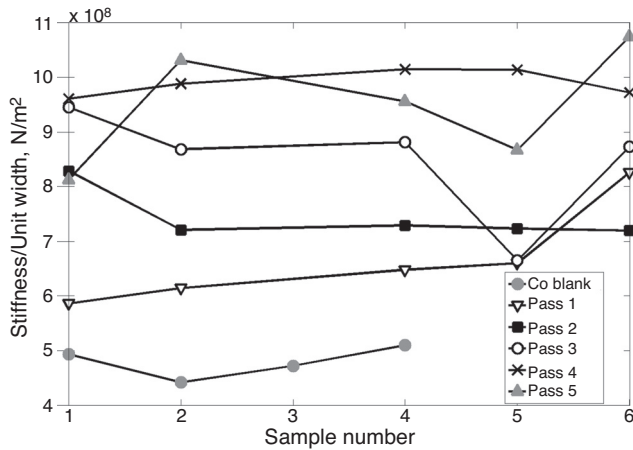
Fig. 10 – Sample stiffness. For the different passes, the sample number corresponds to a change in sample position of .2 inches. The cobalt blank sample numbers do not share this relationship. The stiffness is mainly a function of specimen shape and material composition. A weld's quasi-steady zone should have relatively constant stiffness. The area of greatest consistency in these welds is from samples 2 to 4. The higher stiffness at the beginning and end of these welds is due to the larger weld pools there.

These plots show a large degree of inconsistency for sample 1. This inconsistency is probably caused by the initial weld pool changing the geometry and potentially initializing cracks. Sample 6 is also arguably outside of the quasi-steady state region, as it always fails at a higher moment and higher displacement then the other samples in this series. Further analysis of this data shows a general increase in strength with position (Fig. 12), as well as a linear relationship between moments and displacements at failure (Figs. 12 and 13). The range of measured values, indicated by the error bars (Fig. 12), gives a rough estimate of the variance at each position; the low quality of position one is evidenced by both the high variance in position, and low moment. The high deviations in deflection and load for samples 1 and 6 indicate that these positions are not in the quasi-steady region.

Determination of the quasi-steady region is both subjective and non-trivial. Furthermore, its location seems to vary for our different welds. Defining this region as extending from 30 to 50 mm seems justified, because this area shows a higher degree of consistency (Figs. 9–11) then the surrounding regions, with the different individual welds exhibiting what appears to be random changes in maximum moment, displacement, and stiffness. For the purposes of this study, the region of analysis was chosen to also include sample 6, but not sample 1. Sample 1 was too inconsistent to provide insight into weld behavior (Figs. 9–12); while sample 6, while arguably outside of the quasi-steady state region, still provides consistent data.

Removing sample 1 from the data pool allows investigation into the average behavior of each weld (Fig. 14), with the error bars indicating the ranges of used values. Superimposed on this is the FEA predicted load to failure. As is expected, the increasing number of passes generally results in a stronger
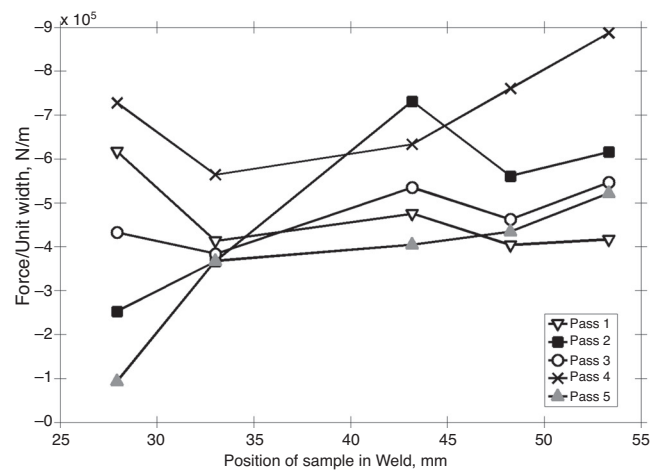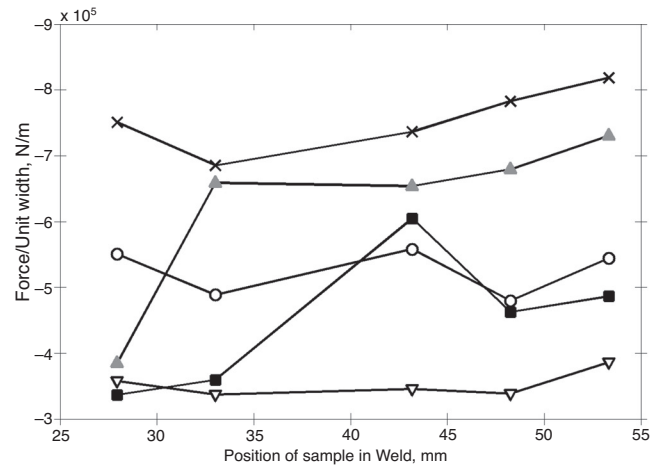

Fig. 11 – Applied loads and deflections at failure. (Top) Applied load at failure vs. sample position. Note the wide disparity of behaviors for the first sample position. From this point onward, the load is still somewhat random, but all welds show an increase in load for the final position. (Bottom) Deflections at failure vs. sample position. Note again the high degree of variation, followed by a more consistent region. Like the above graph of failure loads, all samples show a higher displacement at the final position. This indicates the material here is both stronger and more ductile.

weld (Fig. 14, top), while, surprisingly having little impact on displacements to failure (Fig. 14, bottom). The performance of the cobalt blank in both graphs deviates considerably from predicted; which is expected due to its much smaller grain size reducing its ductility. The differences in displacements by weld are mostly determined by nuances in weld geometry causing stress concentrations, as FEA predictions mirror data (Fig. 14, bottom). The poor performance of the two-pass weld (Weld 2) may be a random result of a poor weld, as the best sample from this weld seems to correlate best with the finite element model.

Investigation into the relationship between moments and displacements inside these welds shows a linear correlation (Figs. 12 and 13). Deviations in geometry (Fig. 2) are thought
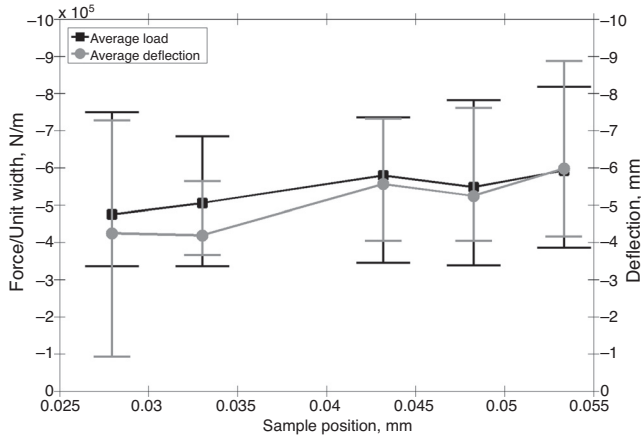
Fig. 12 – Failure loads and deflections by sample position. The error bars indicate the range of recorded values. Several trends are visible, the most striking being the relationship between failure deflections and applied loads. The large deviations at the first sample position indicate that the quasi-steady region does not extend this far for all welds. The increase of weld strength with position, as well as the increased uncertainties at the final position suggests a small quasi-steady state region, potentially only including the samples located between 30.5 mm and 50.8 mm.

to be significant, and may influence this behavior. Changes in the amount of backfilled or empty cracks will also cause such behavior. Alteration of material properties, however, cannot account for observed behavior, since increased strength generally occurs at decreased ductility.
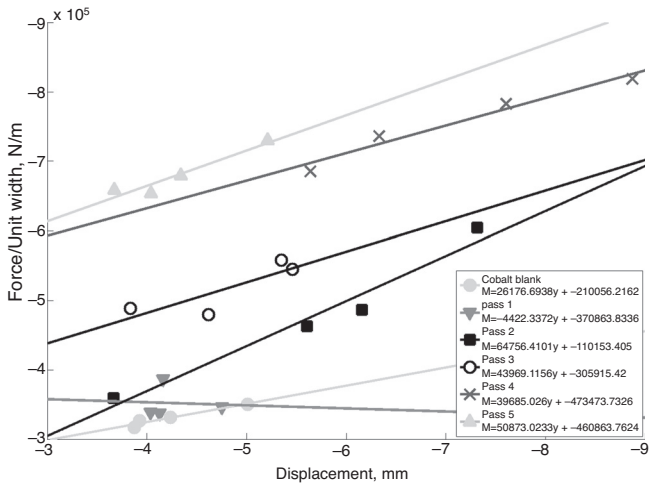

Fig. 13 – Failure loads vs. displacements arranged by weld. Note the clear linear relationship, showing that the most ductile specimens are also the strongest. This is an indication of the effects of random cracking across different samples for the same weld. The most significant outlier is weld pass 1, position 6, which may be an indication that the geometry here is noticeably different to the other samples; an assertion supported by its high stiffness (Fig. 11).
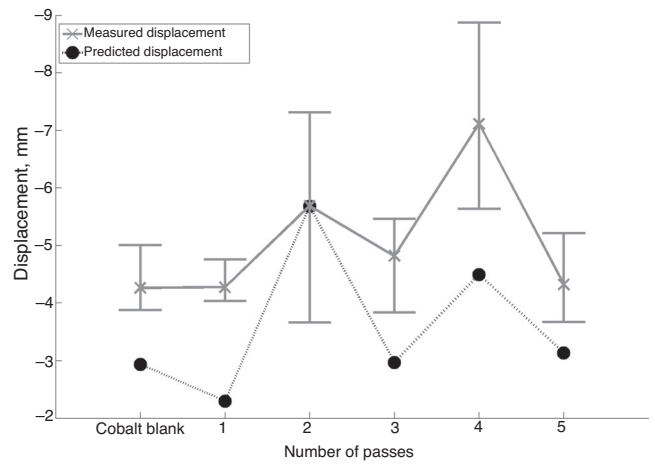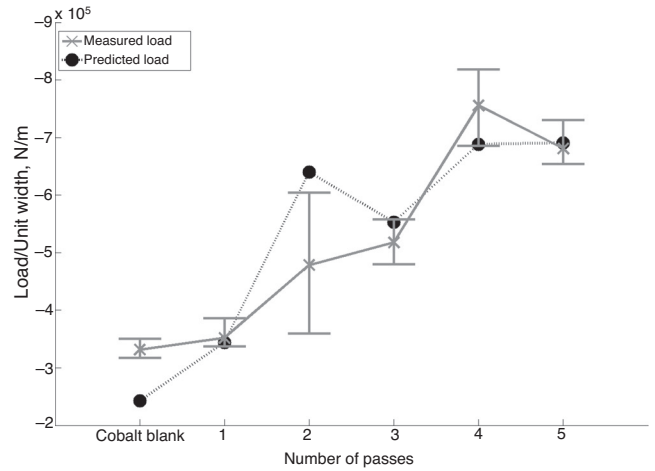

Fig. 14 – Average failure loads and deflections. (Top) Average loads at failure, vs. number of passes. The solid line shows measured values, while the dotted line indicates values predicted by FEA. The error bars indicated the maximum and minimum values measured. The main trend is the increase in strength with the number of passes. This is caused by the addition of material to the weldment. The deviation between measured and predicted values for the cobalt blank was caused by the material not being annealed. (Bottom) Average deflections at failure vs. number of passes. The solid line shows measured values, while the dotted line indicates values predicted by FEA. The difference between predicted and measured values may be due to measurement errors caused by apparatus slip and flex. The high variation at pass 2 is probably caused by influence of cracking.

The displacement at failure is dependent mainly on the sample geometry and on the weld quality. The influence of sample geometry is shown by the correlation of FEA and fracture data. The influence of weld quality is more difficult to define, since the models do not correlate with differing geometries across samples. If the averages (Fig. 14) are considered, we see the average loads at failure for both the two and four pass welds are different than predicted. This deviation is probably caused by the two pass weld being lower than average

quality, and the four pass weld being of excellent quality. The stiffness plot (Fig. 10) supports this by showing approximately constant behavior over each weld; implying that most of the variation for a single weld (Fig. 13) is due to weld quality. This is especially significant for pass 2; it has a very linear stiffness relationship when sample 1 is removed, but huge uncertainties (Fig. 13).

Although weld quality can have a large impact on strength and deflection, the quality is, on average, similar for our welds, which allows for reasonable correlation with FEA results. The effects of cracking are also ameliorated by the maximum stresses occurring away from the central, cracked region.

6. Conclusions

To better understand the nature of Co weldments and to mimic the behavior of the Be–AlSi system, we undertook a systematic welding study involving microscopy, bending tests, and FEA. Cobalt, welded with a silver and copper filler, was the system selected for detailed experimental testing due to the similarity in chemistry, crystal structure, and material properties to the Be-AlSi system. However, once this selection was complete, the concept of "surrogacy" could not be advanced by retaining the original parameters used to weld beryllium with its aluminum–silicon fillers, as this would have resulted in inconsistent, failure prone welds.

To analyze the new welding system, it was important to obtain welding parameters, which result in consistent welds. Although it was possible to weld these two materials together without a parameter study, the results were predictably poor. Furthermore, the random nature of cracking make the usefulness of such an approach dubious. The best option was to perform a parameter study to improve our welds. The most direct determination of weld quality and consistency is strength. It is unlikely that the welding parameters can be meaningfully improved from this point, because the effects of changing parameters is now smaller than the effects of random cracking. Furthermore, consistency is a desirable quality, perhaps more so then strength. Further optimizing these welds to become stronger seems likely to reduce their consistency, which is already imperfect, as these welds are produced by hand. Configuring a machine to produce such welds is possible, although it will be difficult, due to the nuances involved in joining these materials. Ongoing efforts to measure welding power and temperature are a first step to automation.

Utilization of these techniques on the original Be–AlSi welds has not yet been performed. However, this study has seen the evolution of the Co–AgCu welding system from heavily cracked weldments, adhered only by their fillers, to strong consistent weldments, with significant base melting, minimal porosity, manageable cracking and adequate adhesion. It is our assertion that applying similar techniques to the Be welds will allow increased penetration, while reducing cracking and porosity.

Conflicts of interest

The authors declare no conflicts of interest.

REFERENCES

[1] Hausner HH, editor. Beryllium: it's metallurgy and properties. Berkeley/Los Angeles: University of California Press; 1965.
[2] Walsh KA. Beryllium chemistry and processing. Materials Park: ASM International; 2009.
[3] Gale WF, Totemeier TC, editors. Smithells metals reference book. 8th ed. Oxford: Butterworth-Heinemann; 2003.
[4] Jaskula BW. 2011 minerals yearbook: beryllium [advance release]. U S Geol Surv 2013.
[5] Hill MA, Damkroger BK, Dixon RD, Robertson E. Beryllium weldability. In: Materials Weldability Symposium, in Conjunction with ASM Materials Week. 1990 (LA-UR–90-2516).
[6] Castro RG, Jacobson LA, Stanek PW. Beryllium processing technology review for applications in plasma-facing components. LA-12545-MS, UC-904. Los Alamos National Laboratory; 1993, July.
[7] Weismantel EE, Taber KC. Fabrication of beryllium structures by braze-welding, brazing and soldering. In: Proceedings of the Second International Conference. 1964. p. 841–55 (Beryllium Technology; vol. 2).
[8] Brown DW, Varma R, Bourke MAM, Burgardt P, Spooner S, Ely T, et al. Residual strains in a PIGMA welded beryllium ring. Adv X-ray Anal 2001;44:162–7.
[9] Kolanz ME. Introduction to beryllium: uses, regulatory history and disease. Appl Occup Environ Hyg 2001;16(5):559–67.
[10] ASM specialty handbook: nickel, cobalt and their alloys. Materials Park: ASM; 2000.
[11] Cobalt monograph. Brussels: Center D'Information du Cobalt; 1960.
[12] Cobalt facts. Cobalt Development Institute; 2013.
[13] Shedd KB. 2011 minerals yearbook, cobalt [advance release]. U S Geol Surv 2013.
[14] NaBadalung DP, Nicholls JI. Laser welding of a cobalt–chromium removable partial denture alloy. J Prosthetic Dent 1998;73(3):285–90.
[15] MacEntee MI, Hawbolt EB, Zahel JI. The tensile and shear strength of a base metal weld joint used in dentistry. J Dent Res 1981;66(2):154–8.
[16] Black J, Hastings G, editors. Handbook of biomaterial properties. London: Chapman & Hall; 1998.
[17] Buchanan ER. An overview of hardfaced coatings for industrial use. In: Proceedings of the Third International Pump Symposium. 1986, May. p. 91–6.
[18] Riddihough M. Stellite as a wear-resistant material. Tribology 1970;3(4).
[19] Metal prices in the United States through 2010. United States Geological Survey, Special Investigations Report 2012-5188; 2013.
[20] Technical data sheet: Al 718, Rev. 4. Lucas Milhaupt; 2011, April.
[21] Technical data sheet: braze 720 and 721 (VTG), Rev. 6. Lucas Milhaupt; 2008, July.
[22] Lakes R. Viscoelastic materials. Cambridge University Press; 2009.

[23] ASM handbook: vol. 3: alloy phase diagrams. ASM International; 1992.

[24] Okamoto H. Desk handbook phase diagrams for binary alloys. Materials Park: ASM International; 2000.

[25] Karakaya I, Thompson WT. Ag–Co (silver–cobalt). In: Massalski TB, editor. Binary alloy phase diagrams, vol. 1, 2nd ed. Materials Park: ASM International; 1990. p. 25–6.

[26] Murray JL. Ag–Cu (silver–copper). In: Massalski TB, editor. Binary alloy phase diagrams, vol. 1, 2nd ed. Materials Park: ASM International; 1990. p. 28–9.

[27] He XC, Wang H, Liu HS, Jin ZP. Thermodynamic description of the Cu–Ag–Zr system. CALPHAD: Comput Coup Phase Diag Thermochem 2006;30:367–74.

[28] Murray JL, Kahan DJ. Al–Be (aluminum–beryllium). In: Massalski TB, editor. Binary alloy phase diagrams, vol. 1, 2nd ed. Materials Park: ASM International; 1990. p. 125–8.

[29] Pan Z, Du Y, Huang BY, Liu Y, Wang RC. A thermodynamic description of the Al–Be system: modeling and experiment. CALPHAD: Comput Coup Phase Diag Thermochem 2004;28:371–8.

[30] Nikitina GV, Romanenko VN, Ishutinova LN. Energies of mixing in systems containing germanium and silicon with elements of groups III and V. Inorgan Mater 1971;7:41–4.

[31] Udovskii AL, Karpushkin VN, Kozodaeva EA. General algorithm, its mathematical basis and computer autonomic program for calculation of phase diagrams of binary systems, containing p disordered phases of variable and q phases of constant compositions at (p,q) ≤ 10. CALPHAD: Comput Coup Phase Diag Thermochem 1995;19:245–77.

[32] Pan Z, Du Y, Huang B, Xu H, Liu Y, Chen H, et al. Experimental study of the Be–Si phase diagram. J Mater Sci 2006;41: 2525–8.

[33] Du Y, Ran QS, Jin ZP, Effenberg G, Ding W. Optimization and calculation of the Al–Be–Si system. Chin J Met Sci Technol 1992;8:185–91.

[34] Nishizawa T, Ishida K. Co–Cu (cobalt–copper). In: Massalski TB, editor. Binary alloy phase diagrams, vol. 2, 2nd ed. Materials Park: ASM International; 1990. p. 1181–3.

[35] Palumbo M, Curiotto S, Battezzati L. Thermodynamic analysis of the stable and metastable Co–Cu and Co–Cu–Fe phase diagrams. Comput Coup Phase Diag Thermochem 2006;30:171–8.

[36] Plewes JT, Bachmann KJ. The effect of thermomechanical pretreatment on the allotropic transformation in cobalt. Metal Trans 1973;4:1729–34.

[37] Vander Voort GF. Metallography, principles and practice. New York: McGraw-Hill; 1984.

[38] Tian YZ, Wu SD, Zhang ZF, Figueiredo RB, Gao N, Langdon TG. Microstructural evolution and mechanical properties of a two-phase Cu–Ag alloy processed by high-pressure torsion to ultrahigh strains. Acta Mater 2011;59:2783–96.

[39] Meng Q, Guo S, Zhao X, Veintemillas-Verdaguer S. Bulk metastable cobalt in fcc crystal structure. J Alloys Comp 2013;580:187–90.

[40] Seepersad CC, Taleff E, Howell JR, Ely G, Shah S. LANL-UCSD-UT research on weld residual stresses in beryllium. FY09 quarterly report (third quarter: April–June). Los Alamos Engineering Institute; 2009, July.